JOURNAL OF PROPULSION AND POWER
Vol. 23, No. 6, November–December 2007

Nonlinear Response of Plain-Orifice Injectors to Nonacoustic Pressure Oscillations

Megan E. MacDonald,* James V. Canino,† and Stephen D. Heister‡
Purdue University, West Lafayette, Indiana 47907

DOI: 10.2514/1.31189

The response of plain-orifice injectors to finite amplitude nonacoustic pressure pulsations within the downstream chamber was addressed with a series of unsteady axisymmetric Navier–Stokes calculations. Linear theories are reviewed and it is shown that results can be collapsed to a single curve when characterizing the response in terms of a frequency related to the fluid transit time within the orifice passage. Computational results were obtained for a wide range of frequencies, perturbation amplitudes, flow conditions, and orifice designs to quantify the effects of nonlinear fluid mechanics. In general, the simulations all show an unforced response (or self-pulsation) due to instabilities of the vena contracta region lying downstream of the inlet lip. For conditions pertinent to rocket injectors, the nonlinear response is generally bounded by the linear theory (except at high frequencies, in which self-pulsations not accounted for in linear theory remain present). Although a local resonance condition exists when the driving frequency is near the natural/unforced oscillation frequency of the injector, the overall response in this region is still bounded by the linear theory. The effects of orifice rounding and orifice length are also studied parametrically.

Nomenclature

A	=	orifice cross-sectional area
B	=	fluid bulk modulus of elasticity
C	=	capacitance
C_D	=	discharge coefficient
D	=	orifice diameter
$\mathrm{d}m$	=	differential mass
f	=	friction factor, $4\tau_w/q$
g	=	acceleration due to gravity
j	=	$\sqrt{-1}$
K	=	compressibility
K_c	=	fluid/structural interaction factor
K_v	=	valve calibration factor
L	=	orifice length
$\mathcal{L}$	=	inertance
m	=	mass
$\dot{m}$	=	mass flow rate
p	=	pressure
q	=	dynamic pressure determined by the Bernoulli velocity
R	=	resistance
Re	=	Reynolds number
s	=	frequency variable
t	=	time
u	=	axial velocity nondimensionalized by the Bernoulli velocity
V	=	volume
v	=	radial velocity nondimensionalized by the Bernoulli velocity
x	=	axial length along orifice
α	=	phase lag of p'_m behind p'_c
γ	=	ratio of specific heats
ρ	=	density
τ_ω	=	wall shear stress
ϕ	=	phase lag of $\dot{m}'$ behind p'_c
ω	=	frequency, rad/s

Subscripts

c	=	chamber conditions
i	=	injector
l	=	liquid phase
m	=	manifold conditions
rb	=	Reba and Brosilow definition of resistance
v	=	vapor phase

Presented as Paper 4706 at the 42nd AIAA/ASME/SAE/ASEE Joint Propulsion Conference and Exhibit, Sacramento, CA, 9–12 July 2007; received 21 March 2007; revision received 25 April 2007; accepted for publication 25 April 2007.

*Graduate Research Assistant, School of Aeronautics and Astronautics, 315 North Grant Street. Member AIAA.

†Postdoctoral Research Associate, School of Aeronautics and Astronautics, 315 North Grant Street. Member AIAA.

‡Professor, School of Aeronautics and Astronautics, 315 North Grant Street. Associate Fellow AIAA.

I. Introduction

THE injector plays a critical role in defining the performance and stability limits of a liquid rocket engine and remains to be the main component that lacks predictive tools and design models that are not based largely or entirely on the behavior of previous designs. The vast majority of previous instability problems were solved chiefly by making modifications to the injector; it is the component that designers can most readily use to affect the stability characteristics of the engine. The state of the art in injector design relies heavily on empirical data from past designs and linear/empirical models of atomization, secondary atomization, and mixing processes.

The drilled-orifice (plain-orifice) atomizer is commonly used within a variety of liquid rocket injector elements (including the impinging element and the splash plate) and is used as a tangential inlet channel on swirl-type injector elements. Because the design is also used in numerous industrial applications, there is a wealth of literature on the average discharge characteristics and spray properties produced by these simple designs. In particular, [1–4] provide data pertinent to conditions typically encountered in rocket injector applications. In these and numerous other previous works, the discharge coefficient C_D, which is represented as the ratio of measured and theoretical flow rates, is a primary item of interest for the designer. For plain-orifice atomizers, Reynolds number, length/diameter ratio, injection pressure drop, chamber pressure, inlet chamfer, and cavitation all contribute to the measured discharge coefficient. Correlations of experimental measurements [3] and more recent numerical modeling [5] provide mechanisms for the designer

to ascertain the average flow characteristics of the orifice for a given fluid, pressure drop, and orifice geometry.

It has long been understood that the dynamics of the injector element can play a key role in promoting or damping combustion instabilities within liquid rocket engines. Because the injector pressure drop is generally a small fraction of the chamber pressure, small oscillations in chamber pressure lead to large fluctuations in the Δp across the injector. For this reason, the injector functions as an active element within the engine, and its dynamic response is of critical importance to understanding the dynamics of the overall system. The classical analytic treatments [6–11] generally presume a one-dimensional flow within the orifice passage and linearize the governing equations to formulate a second-order dynamic model of the flow process within the passage. Flow resistance due to frictional effects and flow turning, inertance corresponding to the mass of fluid within the orifice passage, and capacitive effects (from fluid compressibility, presence of gas/vapor, or flexing of the injector structure) can generally all be considered in these analyses. Unfortunately, many rocket injector elements are rather short (L/D values less than 5), such that the 1-D assumption is somewhat tenuous in these circumstances. In addition, nonlinear effects of finite amplitude nonacoustic pressure pulsations cannot be addressed in these simplified models.

More recently, a number of works [12–16] have focused on nonlinear multidimensional dynamic simulations to assess these effects. Rump and Heister [12] employed an axisymmetric boundary-element method to assess inviscid dynamics of plain-orifice atomizers and showed that 2-D effects become pronounced at $L/D < 3$. Bazarov and coworkers [8,11] also pointed out that at the high Reynolds numbers characteristic of rocket injectors, unforced pulsations (or self-oscillations) can be observed even under steady inflow and downstream pressure conditions. Hydrodynamic instabilities resulting from oscillations of a vena contracta lying downstream of the inlet lip [5] have been shown to be prominent within the drilled-orifice designs employing sharp inlets. Other laminar instability mechanisms (for example, Kelvin–Helmholz-type modes [14,15] and wake-type instabilities [16] formed behind posts submerged within the outer annular stream) exist in coaxial injectors, which may contribute to the observed unforced pulsations. For these reasons, the nonlinear dynamic response of the injector is highly complex and results from a mixture of unforced and forced responses that are generally amplitude-dependent.

It should be noted that the effect of the injector on combustion instability discussed in the previously cited literature and discussed in this paper is significantly different from the work that focuses on the interaction and dissipation of acoustic energy passing through both long and short ducts [17–22]. Here, the focus is on the hydrodynamics behavior of a liquid, not the acoustics of a gas. Of course, the understanding of both effects is critical to the understanding of combustion instability when coaxial elements are used in rocket engines. However, in the context of plain-orifice rocket injectors, the role of the acoustics in the injector is of secondary importance, due to the low compressibility of the liquid and the modest pressure drops generally employed.

The goal of the present study is to characterize the response of the injector to nonacoustic pressure pulsations for a variety of frequencies, flow properties, and orifice-passage designs. The following section provides a brief review of the linear theory, and the nonlinear model and results are described in subsequent sections.

II. Theoretical Background

It is useful to briefly review the preceding theory in the context of the nonlinear results obtained in the present studies. The previous treatments all presume a one-dimensional flow and linearize convective terms in the momentum equation to provide analytically integrable forms of the governing momentum balance. The Reba and Brosilow [6] treatment is the most comprehensive in that it allows for flow resistance, inertance, liquid compressibility, potential vapor compression in the manifold, and fluid/structure interactions (structural response to pressure changes within the manifold). For these reasons, we will review the results of this model, because degenerate cases provide direct comparisons to other models and to the nonlinear results. In the interest of brevity, only the highlights of the development are described herein; the original works [6,23] contain a more detailed derivation of the governing relationships.

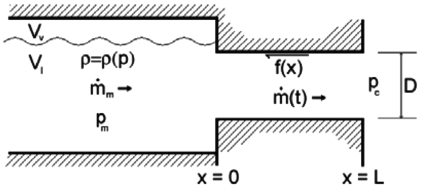

Fig. 1 Injector geometry and nomenclature.

Figure 1 highlights the geometry and flow variables pertinent to the development. Allowing for liquid compressibility introduces the possibility that the instantaneous manifold flow $\dot{m}_m$ can differ from the instantaneous flow within the orifice passage $\dot{m}$. It is also presumed that the manifold volume V_m can generally be composed of both liquid and vapor volumes (V_l and V_v) in the Reba and Brosilow [6] treatment. The unsteady manifold pressure p_m and chamber pressure p_c define the instantaneous flow rates developed in the system. The friction coefficient $f = f(x)$ provides a source of flow resistance within the channel and, allowing for liquid compressibility, we can assume that the liquid density is dependent on pressure $\rho = \rho(p)$ within the manifold. Starting with Newton's second law across a differential liquid element in the injector orifice,

$$Ap - A(p + \mathrm{d}p) - f(x)u\,\mathrm{d}x = \mathrm{d}m\frac{Du}{Dt} \tag{1}$$

We now allow p and u to be composed of a mean component and an oscillating component (i.e., $p = \bar{p} + p'$ and $u = \bar{u} + u'$) and linearize this equation under the assumption of small perturbations. Substituting for the substantial derivative based on its definition, using $u = \dot{m}/(\rho A)$, and realizing that the acceleration of the fluid element will be due only to the time-varying portion of the pressure, Eq. (1) can be rewritten in its perturbation form:

$$-\mathrm{d}p' = \frac{1}{A}\left[\frac{\partial \dot{m}'}{\partial t}\right]\mathrm{d}x + \frac{\dot{m}}{\rho A^2}\left[\frac{\partial \dot{m}'}{\partial x}\right]\mathrm{d}x + \frac{f(x)\dot{m}'}{\rho A^2}\,\mathrm{d}x \tag{2}$$

Equation (2) can be integrated along the length of the injector orifice to derive a relationship between the pressure and mass flow fluctuations. Assuming negligible liquid compressibility within the passage implies that $\mathrm{d}\dot{m}'/\mathrm{d}x = 0$. Reba and Brosilow [6] introduced a flow resistance that is the slope of the pressure drop versus the mass flow characteristic: $R_{\mathrm{rb}} = \mathrm{d}\Delta p/\mathrm{d}\dot{m}$. This definition differs from that currently used in other contexts, as will be noted in subsequent discussions. Using this definition and the preceding assumptions, Eq. (2) can be cast as

$$p'_m - p'_c = \mathcal{L}\frac{\mathrm{d}\dot{m}'}{\mathrm{d}t} + R_{\mathrm{rb}}\dot{m}' \tag{3}$$

where $\mathcal{L} = L/A$ is defined as the inertance in analogy to the inductance within electrical R-$\mathcal{L}$-C circuits that are governed by an equation identical in form to Eq. (3). Fluctuations in the manifold pressure p'_m can be related to mass flow pulsations by considering the overall compressibility of the fluid system. The mass of fluid in the manifold, $m_m = \rho_l V_l + \rho_v V_v$, can be written in terms of gas and liquid density/volume sensitivities to changes in the manifold pressure:

$$\frac{\mathrm{d}m_m}{\mathrm{d}p_m} = \rho_l\frac{\mathrm{d}V_l}{\mathrm{d}p_m} + V_l\frac{\mathrm{d}\rho_l}{\mathrm{d}p_m} + \rho_v\frac{\mathrm{d}V_v}{\mathrm{d}p_m} + V_v\frac{\mathrm{d}\rho_v}{\mathrm{d}p_m} \tag{4}$$

The liquid compressibility can be expressed in terms of the bulk modulus of elasticity for the liquid, $B = \rho_{\mathrm{lu}}\mathrm{d}p_m/\mathrm{d}\rho_l$, where ρ_{lu} is the uncompressed density. For the vapor lying within the manifold, the compressibility factor is defined as $\rho_v K = \mathrm{d}\rho_v/\mathrm{d}p_m$. Substituting for B and K and using the fact that $V_v = V_m - V_l$, we obtain

$$\frac{\mathrm{d}m_m}{\mathrm{d}p_m} = \rho_l \frac{\mathrm{d}V_m}{\mathrm{d}p_m} - \rho_l \frac{\mathrm{d}V_v}{\mathrm{d}p_m} + V_l \frac{\rho_l}{B} + V_v \rho_v K \tag{5}$$

where we have also assumed that $\rho_v \ll \rho_l$.

Even further simplification results from the definition of a constant K_c, described by Reba and Brosilow [6] as "a function of the shape, wall thickness, and materials of construction of the injector head" and defined by $\mathrm{d}V_m/\mathrm{d}p_m = K_c V_m$. Also, if the expansion and contraction of any vapor bubbles in the manifold is assumed to be isentropic, they will obey the equation $p_m V_v^{\gamma} = \text{const}$, which implies

$$\frac{\mathrm{d}V_v}{\mathrm{d}p_m} = -\frac{V_v^{\gamma}}{p_m \gamma V_v^{\gamma-1}} = -\frac{V_v}{\gamma p_m} \tag{6}$$

Using Eq. (6) and the definition of K_c, Reba and Brosilow [6] obtained

$$\frac{\mathrm{d}m_m}{\mathrm{d}p_m} = \rho_l K_c V_m + \rho_l \frac{V_v}{\gamma p_m} + V_l \frac{\rho_l}{B} + V_v \rho_v K \tag{7}$$

Equation (7) gives the overall capacitance of the manifold in that it describes the change in mass within the manifold as a function of changing manifold pressure. If we define an overall capacitance $C = \mathrm{d}m_m/\mathrm{d}p_m$ and assume a negligible mass of vapor in the manifold when compared with the liquid mass, then

$$C = \rho_l V_m \left[K_c + \frac{1}{\gamma p_m} \frac{V_v}{V_m} + \frac{V_l}{V_m} \frac{1}{B} + \frac{\rho_v}{\rho_l} \frac{V_v}{V_m} K \right] \tag{8}$$

Assuming that C is a constant for small perturbations in pressure, differentiation of the definition of C gives a connection between the unsteady component of the manifold pressure and mass:

$$\frac{\mathrm{d}m_m}{\mathrm{d}t} = C \frac{\mathrm{d}p_m}{\mathrm{d}t} \tag{9}$$

However, the change in mass in the manifold is $\mathrm{d}m_m/\mathrm{d}t = \dot{m}_m - \dot{m}$, and steady state $\dot{m}_m$ and $\dot{m}$ must have a difference of zero, otherwise mass would be continuously increasing or decreasing in the manifold. So the difference must be attributed solely to the perturbation quantities, giving

$$\frac{\mathrm{d}m_m}{\mathrm{d}t} = \dot{m}'_m - \dot{m}' \tag{10}$$

Combining Eqs. (9) and (10) and noting that the perturbation part of the pressure is the only part that is time-dependent gives

$$C \frac{\mathrm{d}p'_m}{\mathrm{d}t} = \dot{m}'_m - \dot{m}' \tag{11}$$

Equations (3) and (11) provide two relationships for p'_m and $\dot{m}'$, respectively, but an additional relationship is required for the unsteady flow into the manifold. Reba and Brosilow [6] introduced a *valve calibration factor* defined as $K_v = -\dot{m}'_m/p'_m$, which is related to the change in valve flow coefficient as a function of pressure drop. Using this implementation, Eq. (11) becomes

$$C \frac{\mathrm{d}p'_m}{\mathrm{d}t} = -K_v p'_m - \dot{m}' \tag{12}$$

Physically, systems with high K_v would be highly responsive and $\dot{m}'_m$ would change nearly instantaneously with variations in manifold pressure. The other limit, $K_v = 0$, corresponds to a completely unresponsive flow that can be obtained by using flow-limiting devices (cavitating venturis) or constant-volume flow devices (an idealized pump), assuming negligible upstream capacitance. Equations (3) and (12) provide a two-equation system for p'_m and $\dot{m}'$ that can be solved using Laplace transforms subject to initial conditions $p'_m(0) = 0$, $\mathrm{d}p'_m(0)/\mathrm{d}t = 0$, $\dot{m}'(0) = 0$, and $\mathrm{d}\dot{m}'(0)/\mathrm{d}t = 0$. Assuming that the downstream pressure is a waveform $p'_c e^{i\omega t}$, the resulting solutions for the magnitude and phase of the manifold pressure and injector flow are

$$\left|\frac{p'_m}{p'_c}\right| = \frac{1}{\sqrt{(R_{\mathrm{rb}}K_v + 1 - \mathcal{L}C\omega^2)^2 + (\mathcal{L}K_v + R_{\mathrm{rb}}C)^2\omega^2}}$$
$$\alpha = \tan^{-1}\left(\frac{(\mathcal{L}K_v + R_{\mathrm{rb}}C)\omega}{R_{\mathrm{rb}}K_v + 1 - \mathcal{L}C\omega^2}\right) \tag{13}$$

$$\left|\frac{\dot{m}'}{p'_c}\right| = \frac{\sqrt{C^2\omega^2 + K_v^2}}{\sqrt{(R_{\mathrm{rb}}K_v + 1 - \mathcal{L}C\omega^2)^2 + (\mathcal{L}K_v + R_{\mathrm{rb}}C)^2\omega^2}}$$
$$\phi = \tan^{-1}\left(\frac{C\omega}{K_v}\right) - \tan^{-1}\left(\frac{(\mathcal{L}K_v + R_{\mathrm{rb}}C)\omega}{R_{\mathrm{rb}}K_v + 1 - \mathcal{L}C\omega^2}\right) \tag{14}$$

where α and ϕ are the phase angle of the manifold pressure and injector mass flow, respectively. Equations (13) and (14) provide the most general 1-D linearized result accounting for flow resistance, inertance, and a variety of capacitive effects. Most previous investigations presumed that the manifold is essentially an infinite mass source that corresponds to a limiting condition of $K_v \to \infty$ in the preceding relations. In this limit, manifold pressure oscillations vanish (p'_m magnitude) and the mass flow pulsation in the orifice passage becomes

$$\frac{\dot{m}'}{p'_c} = \left[\frac{-1}{R_{\mathrm{rb}} + \mathcal{L}j\omega}\right] \tag{15}$$

Under the infinite mass source assumption, capacitive effects vanish altogether. Equation (15) can be reconciled with previous results [6,7] by accounting for the differences in the definition of the flow resistance.

Reba and Brosilow [6] defined $R_{\mathrm{rb}} = \mathrm{d}\Delta p/\mathrm{d}\dot{m}$, but $\Delta p = \rho u^2/2 = \rho\dot{m}^2/2C_D^2\rho^2A^2$ and so $R_{\mathrm{rb}} = \dot{m}/C_D^2\rho A^2$. In most other sources, the resistance is defined as $R = \Delta p/\dot{m}^2$ or $R = 1/2C_D^2\rho A^2$. Comparing these results, we can see that $R_{\mathrm{rb}} = 2\dot{m}R$ and Eq. (15) can be written as

$$\frac{\dot{m}'}{p'_c} = \left[\frac{-1}{2\dot{m}R + \mathcal{L}j\omega}\right] \tag{16}$$

which is equivalent to results reported in previous studies [6,7]. Equation (16) can be written in terms of the overall admittance if mass flow and pressure perturbations are nondimensionalized against the mean flow rate and mean orifice pressure drop, respectively. Performing this nondimensionalization gives the working form of the injector admittance that is most commonly seen in previous works:

$$\frac{\dot{m}'/\dot{m}}{p'_c/\Delta p} = \frac{-\Delta p}{2\Delta p + \dot{m}\mathcal{L}j\omega} \tag{17}$$

In terms of the mean flow rate produced in the device, the resulting magnitude and phase shifts are then

$$\left|\frac{\dot{m}'/\dot{m}}{p'_c/\Delta p}\right| = \frac{\dot{m}/2}{\sqrt{\dot{m}^2 + (C_D^2\rho A^2\mathcal{L}\omega)^2}} \qquad \phi = -\tan^{-1}\left(\frac{C_D^2\rho A^2\mathcal{L}\omega}{\dot{m}}\right) \tag{18}$$

Figure 2 shows typical results for a baseline injector with an injector pressure drop of $\Delta p = 0.26$ MPa, $D = 0.2$ cm, $L/D = 3$, $\bar{p}_c = 5$ MPa, and $\rho = 800$ kg/m^3. The overall response is analogous to a linear oscillator. At low frequencies, there is negligible magnitude loss and the phase shift is near zero (i.e., the injector oscillates in phase with the input signal). At intermediate frequencies, the resistance term has a large impact on the response of the injector and a diminished magnitude is observed. At very high frequencies, the injector is unable to respond to the input signal and the magnitude of the fluctuations approaches zero. The phase shift has a similar rolloff behavior in which at high frequencies, $\dot{m}'$ lags p'_c by 90 deg. As L/D increases, the phase lag grows more quickly as the time the flow spends in the orifice passage increases.

The response curves show an interesting variation with the orifice discharge coefficient. At a given frequency, as C_D decreases, the

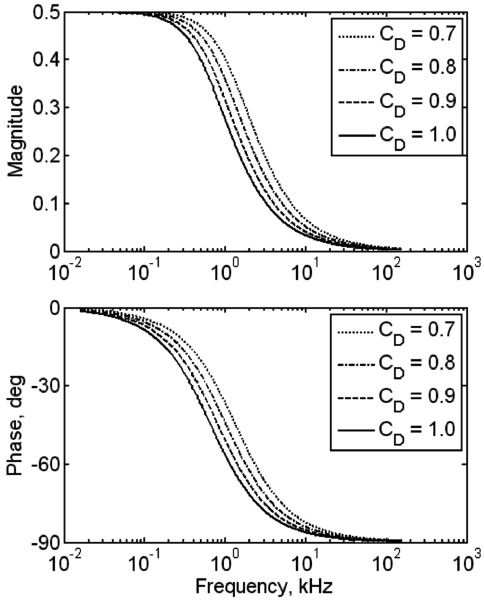

Fig. 2 Injector response with resistance ($L/D = 3$).

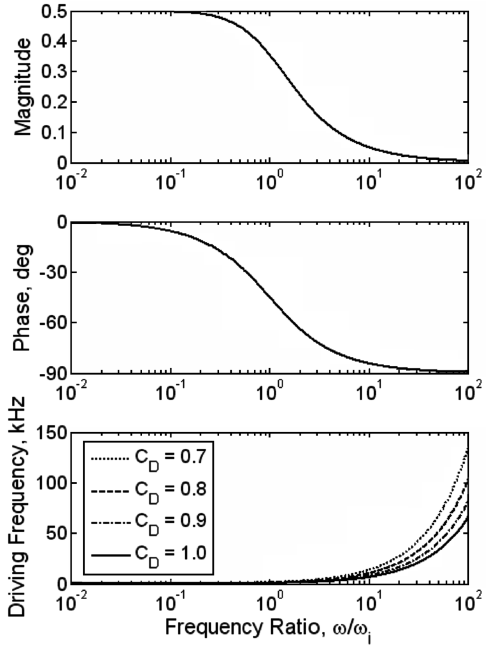

Fig. 3 Universal amplitude/phase response in terms of injector frequency ratio ω/ω_i.

magnitude of the response actually gets larger. One can think of this in terms of the vena contracta that is formed downstream of the orifice lip. When a sharp inlet is used, a larger vena contracta region is present, thereby reducing the effective length of the orifice downstream of this recirculating region. This decreased length results in a decrease in the effective inertance and actually increases the magnitude response.

It is useful to cast the results of the linear analysis in terms of an injector frequency that is representative of the time for a fluid element to traverse the length of the passage under mean flow conditions. Physically, the quantity $\dot{m}/\rho ALC_D^2$ in Eq. (18) represents a frequency related to this travel time. If we let this group be represented by an injector frequencyω_i,

$$\omega_i = \frac{\dot{m}}{\rho ALC_D^2} \tag{19}$$

then the response function can be simplified to

$$\frac{\dot{m}'/\dot{m}}{p_c'/\Delta p} = \frac{0.5}{1 + j\frac{\omega}{\omega_i}} \tag{20}$$

By casting results in this form, a *universal* response curve, valid for any discharge coefficient and orifice geometry, can be obtained. Figure 3 provides this universal response curve in terms of the applicable frequency ratio ω/ω_i. However, because C_D is included in ω_i, ω/ω_i varies with C_D; this relationship is also plotted in Fig. 3.

III. Computational Model

The nonlinear simulations were performed using an axisymmetric laminar incompressible flow solver based on the marker and cell formulation [24]. Although the high Reynolds numbers characteristic of rocket injector flows (Reynolds numbers between 10,000 and 200,000) will create turbulent flowfields, the dominant feature leading to unsteadiness in these flows is the large laminar separation that forms the vena contracta downstream of the lip. The flow into the orifice entrance is strongly accelerated, and turbulence is expected to have the greatest impact downstream of the vena contracta. Time-accurate simulations of the Reynolds-averaged Navier–Stokes (RANS) equations is an area of study in and of itself, and the computational cost of higher-resolution direct numerical simulation or large eddy simulation prohibited consideration of these schemes for the present parametric studies. Because the laminar unsteady behavior is much more amenable to study, parallels the linear theory, and is the source of the major unsteadiness in the flow, we focus on this for the present set of computations. The two-dimensional axisymmetric code uses a finite volume formulation of the marker and cell method, which incorporates a staggered grid to prevent odd–even pressure splitting [25]. The axisymmetric Navier–Stokes equations can be written as

$$\frac{\partial(rv)}{\partial r} + \frac{\partial(ru)}{\partial z} = 0 \tag{21}$$

$$\frac{\partial(ru)}{\partial t} + \frac{\partial(ruv)}{\partial r} + \frac{\partial(ru^2)}{\partial z} = -r\frac{\partial p}{\partial z} + \frac{1}{Re}\left[\frac{\partial}{\partial r}\left(r\frac{\partial u}{\partial r}\right) + \frac{\partial^2(ru)}{\partial z^2}\right] \tag{22}$$

$$\frac{\partial(rv)}{\partial t} + \frac{\partial(rv^2)}{\partial r} + \frac{\partial(rvu)}{\partial z} = -r\frac{\partial p}{\partial r} + \frac{1}{Re}\left[r\frac{\partial}{\partial r}\left(\frac{1}{r}\frac{\partial(rv)}{\partial r}\right) + \frac{\partial^2(rv)}{\partial z^2}\right] \tag{23}$$

where u and v are the axial and radial velocity components aligned with the z and r directions, respectively. Furthermore, Re is the Reynolds number based on the diameter of the drilled orifice and the Bernoulli velocity determined from the imposed pressure drop. For these incompressible calculations, a typical segregated scheme is used whereby the pressure is determined implicitly by a Poisson equation and then the velocities are updated.

To determine the Poisson equation, the continuity equation is discretized as

$$(\boldsymbol{V}\cdot\boldsymbol{n})_1\,\mathrm{d}A_1 + (\boldsymbol{V}\cdot\boldsymbol{n})_2\,\mathrm{d}A_2 + (\boldsymbol{V}\cdot\boldsymbol{n})_3\,\mathrm{d}A_3 + (\boldsymbol{V}\cdot\boldsymbol{n})_4\,\mathrm{d}A_4 = 0 \tag{24}$$

where the subscripts 1, 2, 3, and 4 refer to a cell face.

Furthermore, the radial momentum equation can be discretized as

$$v^{n+1} = v^n + \frac{\Delta t}{r_o \Delta V}(N_1 - N_3 + N_2 - N_4) + \frac{\Delta t}{\Delta V}[(P^{n+1}|s|n_y)_1 - (P^{n+1}|s|n_y)_3 + (P^{n+1}|s|n_y)_2 - (P^{n+1}|s|n_y)_4] \tag{25}$$

In Eq. (25), the values of N are the flux terms defined as

$$N_k = |S_k|\left\{(r\boldsymbol{V}\cdot\boldsymbol{n}v)_k - \frac{1}{Re_k}\left(\frac{\partial(rv)}{\partial z}n_x + \frac{r_o}{r}\frac{\partial(rv)}{\partial r}n_y\right)_k\right\} \quad (26)$$

where k refers to computations performed at the appropriate control volume face and r_o is the radius to the center of the control volume.

Additionally, the discrete axial momentum equation is

$$u^{n+1} = u^n + \frac{\Delta t}{r_o \Delta V}(M_1 - M_3 + M_2 - M_4) + \frac{\Delta t}{\Delta V}[(P^{n+1}|s|n_x)_1 - (P^{n+1}|s|n_x)_3 + (P^{n+1}|s|n_x)_2 - (P^{n+1}|s|n_x)_4] \quad (27)$$

where

$$M_k = |S_k| r_k\left\{(\boldsymbol{V}\cdot\boldsymbol{n}u)_k - \frac{1}{Re_k}\left(\frac{\partial u}{\partial z}n_x + \frac{\partial u}{\partial r}n_y\right)_k\right\} \quad (28)$$

The pressure Poisson equation is formed by substituting the discretized momentum equations (25) and (27) into the discretized continuity equation (24). Once this process is performed, the Poisson equation takes the following form:

$$A_1(i,j)P_{i+1,j-1} + A_2(i,j)P_{i+1,j} + A_3(i,j)P_{i+1,j+1} + A_4(i,j)P_{i,j-1} + A_5(i,j)P_{i,j} + A_6(i,j)P_{i,j+1} + A_7(i,j)P_{i-1,j-1} + A_8(i,j)P_{i-1,j} + A_9(i,j)P_{i-1,j+1} = R(i,j) \quad (29)$$

In the Poisson equation, A is simply a function of the geometry of the grid and $R(i, j)$ includes all of the flux terms for both the radial and axial momentum equations. Once the pressure is obtained by solving the Poisson equation, the axial and radial velocities are determined explicitly from the discrete momentum equations. The scheme has been shown to be second-order accurate [14].

IV. Results

Grid-function convergence studies were performed to verify that the solutions are independent of the mesh that was selected. To confirm convergence, pressure fields were averaged along various gridlines and compared for various meshes. Figure 4 provides a sample pressure profile indicating that a 171×90 grid provides adequate resolution of the pressure field. In Fig. 4, the top plot indicates the grid line for which the pressure was time-averaged, and the bottom plot shows the time-averaged pressure along that grid line.

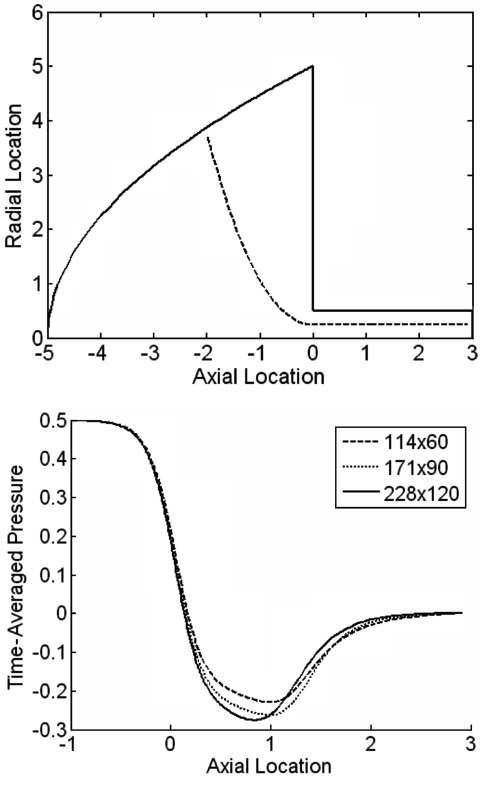

Fig. 4 Typical time-averaged pressure profiles for several meshes.

Time accuracy of the scheme was insured by using a dimensionless time step of 0.00066 in the simulations. Previous benchmarking of the code [23] has verified the temporal accuracy of the scheme. Standard boundary conditions were applied to insure that there was no slip on the solid walls and symmetry along the $r = 0$ line in the mesh. A constant-pressure inflow boundary condition and flow angle were used, and flow velocities along this surface were extrapolated from within the mesh. At the outflow boundary, an oscillatory pressure was imposed:

$$p = \bar{p}(1 + \varepsilon \sin \omega t) \quad (30)$$

where the unsteadiness was prescribed in terms of the amplitude ε and frequency ω of the input signal.

The self-oscillations induced by the unstable vena contracta are illustrated in the velocity field history presented in Fig. 5. Steady inflow and outflow conditions (consistent with those used in Fig. 2) were used in this simulation. The main recirculation zone is composed of multiple small recirculation cells that grow as they convect downstream. The growing cells cause a vortex to be shed from the reentrant region and the growth process begins anew. Under these conditions, a single cycle of the natural oscillation is shown to take approximately 420 ms, which gives a natural frequency of $\omega_n = 2.38$ kHz.

As the unstable vena contracta oscillates, the vortices in the separated region cause the displacement thickness of the boundary layer to vary with time. Because the mass flow rate is proportional to the displacement thickness in an incompressible flow, the mass flow rate also varies in time. This time-dependent resistance in the passage leads to pulsations or self-oscillations in the discharge coefficient. Because of the lack of compressibility in the liquid, the mass flow at the inlet and outlet are the same at all times, but both change in time with the oscillation of the vena contracta.

Although the mean discharge coefficient does change slightly with the imposed downstream pressure, an approximate ω_i value from Eq. (19) for this baseline injector is 7.0 kHz, based on a mean discharge coefficient of 0.78. The relationship between ω_n and ω_i is dependent on the orifice L/D. Table 1 provides the relationship between these two frequencies for the injection conditions and flow properties noted in the baseline case. As shown in the table, both frequencies tend to decrease with increased injector length, and their ratio lies in the range of $0.1 < \omega_n/\omega_i < 0.35$ over the range investigated.

Injector response is computed by investigating the time history of the dimensionless orifice mass flow (discharge coefficient) for a given assumed forcing amplitude and frequency. Because the orifice flow is hydrodynamically unstable due to the presence and instability of the vena contracta, oscillatory solutions are obtained even without forcing. The baseline conditions are the same as those employed in the linear analysis results, as described in Fig. 2. The nonlinear frequency response of this injector was analyzed for various perturbation amplitudes. These studies were carried out at 18 different frequencies, ranging from one-tenth to 100 times the natural frequency of the orifice (0.1 to $100\omega_n$). In addition, the effect of the Reynolds number, inlet radius, and injector length were studied.

Figure 6 depicts a typical history of the dimensionless mass flow variation about the mean, $C_D' = C_D - \bar{C}_D$, and the input downstream pressure signal p'. In this case, the downstream pressure is oscillated at a frequency of 0.24 kHz ($\omega = 0.1\omega_n$) with an amplitude of 40% of the mean pressure drop imposed on the orifice ($\varepsilon = 0.1$). At this low driving frequency, the mass flow history closely follows the input signal, but higher-frequency oscillations corresponding to the natural frequency of the injector are also present. In this case, the natural pulsations are of a much smaller amplitude than the imposed oscillation, as indicated in the mass flow history.

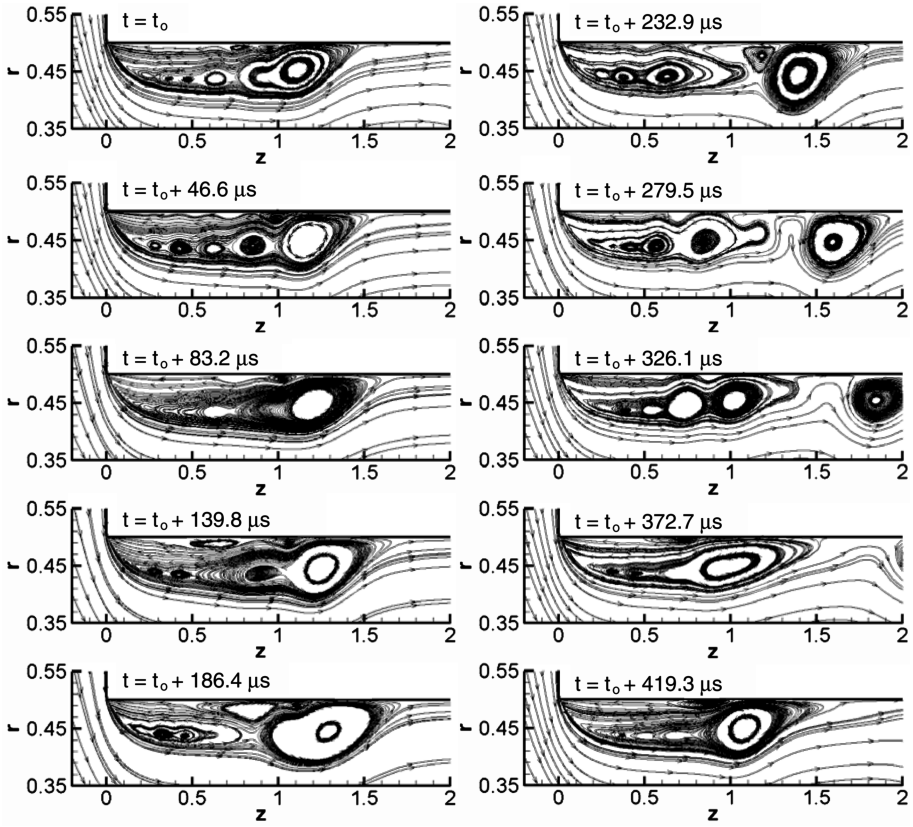

Fig. 5 Instantaneous streamlines during a single cycle of an injector unforced pulsation for $\Delta p = 0.26$ MPa, $D = 0.2$ cm, $L/D = 3$, $\bar{p}_c = 5$ MPa, $\rho = 800$ kg/m^3, and $Re = 25,500$.

The frequency content of the mass flow perturbation was assessed by performing a fast Fourier transform (FFT) on the unsteady signals. The unsteady signal typically composed at least 50 flow-through cycles and sometime as many as 100 flow-through cycles. In all cases, enough flow-through cycles were used to achieve adequate resolution of the dynamics. Results for both the imposed pressure signal and the mass flow response are depicted in Fig. 7. As expected, the pressure signal depicts a single peak at the imposed frequency. The mass flow spectrum shows a complex response that is dominated by the imposed frequency (0.24 kHz) and the natural frequency (2.4 kHz). Figure 7 also shows peaks in response at the 1.2-kHz subharmonic and 4.8- and 7.2-kHz second and third harmonics of the natural frequency.

Figures 8 and 9 depict results analogous to Figs. 6 and 7 for the baseline injector with a driving frequency coincident with the natural frequency peak ($\omega = \omega_n$) and the same amplitude of the pressure perturbation. Figure 8 depicts the mass flow pulsation showing a low beat frequency formed by the drift in the phase of the input signal relative to the natural response. The overall amplitude of the mass flow perturbations are diminished when compared with the lower-frequency case (Fig. 6), in accordance with the linear theory. The FFT of the mass flow perturbation for this case is shown in Fig. 9. Here, a strong peak is noted at the driving/natural frequency, with

Table 1 Relationship between natural oscillation frequency ω_n and injector frequency ω_i for baseline injection conditions

L/D	ω_n, kHz	ω_i, kHz	ω_n/ω_i
2	2.85	10.93	0.261
3	2.38	7.06	0.337
3.5	2.17	6.21	0.349
4	1.79	5.39	0.332
5	1.08	4.32	0.250
6	0.64	3.61	0.177
8	0.38	2.74	0.139

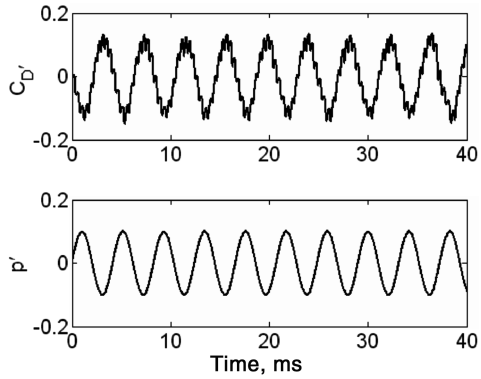

Fig. 6 Oscillating mass flow results for a driving pressure at 0.24 kHz and $\varepsilon = 0.1$.

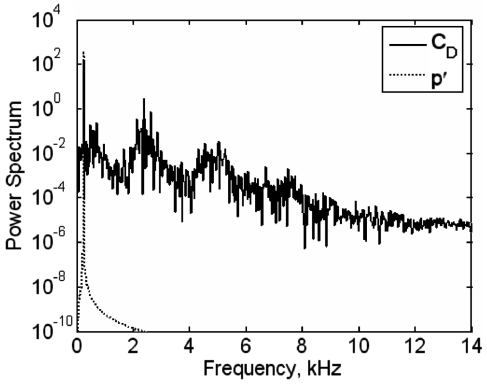

Fig. 7 FFT of the C_D' signal for driving pressure at 0.24 kHz and $\varepsilon = 0.1$.

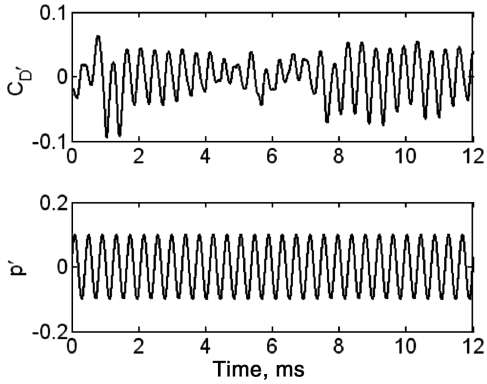

Fig. 8 Oscillating mass flow results for a driving pressure at 2.42 kHz and $\varepsilon = 0.1$.

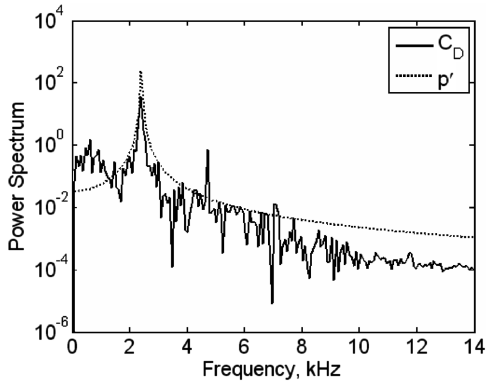

Fig. 9 FFT of the C_D' signal for driving pressure at 2.42 kHz and $\varepsilon = 0.1$.

local peaks at the subharmonic and higher harmonic modes of this frequency.

A total of 18 individual driving frequencies were investigated in the manner noted in Figs. 6–9 to map out the overall frequency response of the baseline injector. A Fourier decomposition was employed to extract the power content of the amplitude of the natural oscillation relative to the overall mass flow pulsation. Both magnitude and phase responses were investigated and compared against results from the linear theory. The magnitude and phase of the computational fluid dynamics (CFD) driving frequency were determined by dividing the complex Fourier coefficient of the discharge coefficient associated with the fundamental driving frequency by the complex Fourier coefficient of the pressure associated with the driving frequency. Furthermore, the magnitude and phase of the CFD natural frequency were determined by dividing the complex Fourier coefficient of the discharge coefficient associated with the fundamental natural frequency by the complex Fourier coefficient of the pressure associated with the driving frequency. Harmonics in the discharge coefficient were neglected when determining the amplitude and phase presented herein, because the power associated with them is at least two orders of magnitude smaller than the power associated with the fundamental natural and driving frequencies.

Figure 10 provides a summary of the nonlinear frequency response of the baseline injector subjected to a forcing at 40% of the mean pressure drop across the orifice. In Fig. 10, + represents the magnitude of the response attributable to the natural oscillations/self-pulsations within the injector, × represents the response to the driving frequency obtained via the Fourier decomposition [23], and * indicates the sum of the forced and natural contributions obtained by adding the magnitudes of the Fourier coefficients associated with the forced excitation frequency and the natural frequency as determined by assessing unforced behavior. Because the two signals will drift relative to each other, the maximum value of the signal in which the forced and natural frequencies are in phase represents the upper

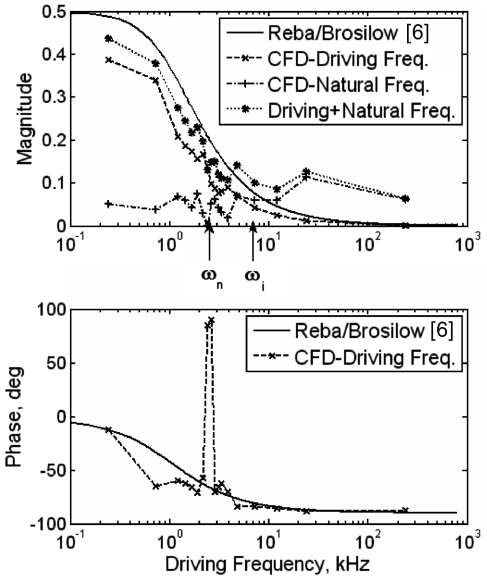

Fig. 10 Comparison of linear and nonlinear responses for $\varepsilon = 0.1$ ($\bar{C}_D = 0.78$).

bound on the nonlinear amplitude that is plotted in Fig. 10. Additionally, the results of the linear theory from Eq. (18) are plotted as a solid line in Fig. 10.

Figure 10 provides the interesting and important result that the nonlinear results are bounded by the linear theory for a good portion of the frequency spectrum, even for the worst case considered when the natural and forced waves are in phase. At low frequencies, the linear results substantially overpredict the responsiveness of the injector. Clearly, multidimensional flow effects contribute to these differences, because the long wavelengths consistent with the low frequencies are particularly susceptible to these effects. Only at high frequencies (approximately when $\omega > \omega_i$) does the nonlinear response exceed the linear values. In this region, the nonlinear response is dominated by the natural pulsations of the vena contracta.

At the condition in which $\omega = \omega_n$, we arbitrarily assumed that all of the response was attributed to the driven value, and as a result, the component attributed to the natural oscillation (+ in Fig. 10) goes to zero at this location. It is interesting to note that the overall nonlinear response does show a local peak in the region near $\omega = \omega_n$, but a large growth in the amplitude of the oscillation is not observed. Apparently, the energy content attributable to oscillations of the vena contracta is quite bounded and this provides important information relative to the stability of injectors operating near this potentially resonant condition. The radial extent of the vena contracta is bounded in the observations of the unsteady streamlines (Fig. 5) and this provides a bound for the resultant mass flow pulsation.

Figure 10 shows that the phase of the nonlinear computations is below that predicted by the linear theory. In the region in which the driving frequency is very near the natural frequency, substantial phase leads are noted in accordance with the constructive interference of the two signals. Both linear and nonlinear results approach zero phase shift at low frequencies and −90-deg phase shift at very high frequencies, in accordance with linear theory.

Although the response plot in Fig. 10 was completed for a driving amplitude of 40% of the pressure drop across the injector, two other driving amplitudes were also considered: $\varepsilon = 0.15$ and 0.2, which correspond to 60 and 80% of the pressure drop across the orifice.

Figure 11 shows a similar magnitude frequency response as the more modest forcing within Fig. 10 conditions. Keeping in mind that the magnitudes are nondimensionalized by the driving pressure amplitude, the component of the signal attributed to the natural frequency is similar in magnitude to the result shown in Fig. 10. Subtle differences in the behavior near the resonant condition are noted in the driven component of the response. The phase response in Fig. 11 for the 60% perturbation in orifice pressure drop is very similar to that for the 40% Δp forcing noted in Fig. 10.

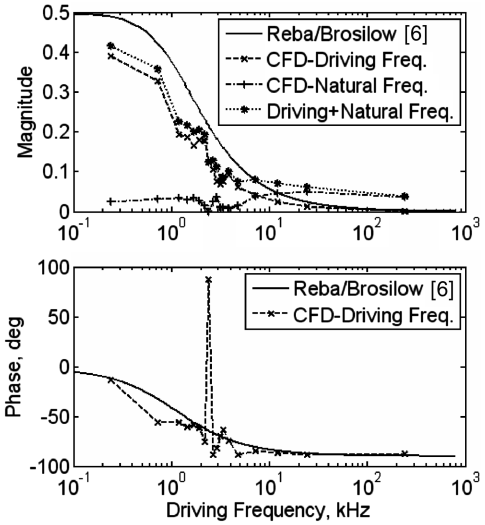

Fig. 11 Comparison of linear and nonlinear responses for $\varepsilon = 0.15$ ($\bar{C}_D = 0.77$).

At the 80% Δp forcing, shown in Fig. 12, similar trends in the magnitude response are noted. The natural oscillations become an increasingly smaller contribution to the total response and are generally insensitive to the level of forcing. Figure 12 does show a substantial difference in the phase of the signal near the resonant condition, in which $\omega = \omega_n = 2.4$ kHz. In this case, the large phase lead in this region is no longer present and the overall phase response is bounded by the linear results over the bulk of the frequency range.

Figure 13 shows a compilation of the response plots for all amplitudes considered. The Reba and Brosilow [6] linear curve was calculated for an average C_D for all three cases of $C_D = 0.77$. The overall magnitude (lines are represented by * in Figs. 10–12) is compared in the upper part of the figure, and the phase response is compared in the lower part. The dimensionless magnitude tends to decrease over the entire frequency space as the perturbation amplitude is increased. The phase response for the three distinct ε values is similar over the bulk of the frequency space. For the lower-amplitude driving conditions ($\varepsilon = 0.1$ and 0.15), a phase lead is noted in the region near the resonant condition; this behavior vanishes at the higher-amplitude forcing.

The effect of inlet radius was also studied parametrically for the baseline geometry at the resonant frequency condition. Although the baseline case has a very small radius of 0.01 mm, an actual injector will have a finite radius of curvature. The corner-radius-to-orifice-

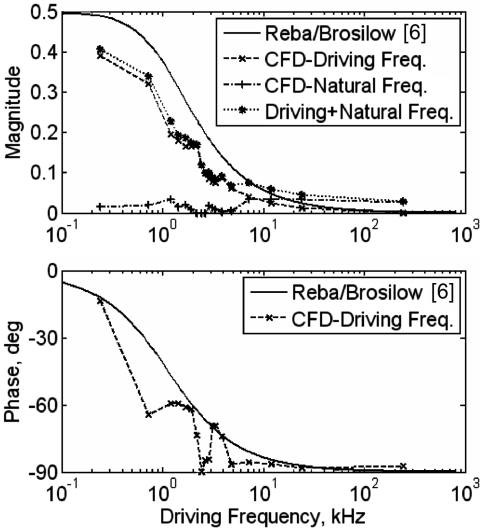

Fig. 12 Comparison of linear and nonlinear responses for $\varepsilon = 0.2$ ($\bar{C}_D = 0.77$).

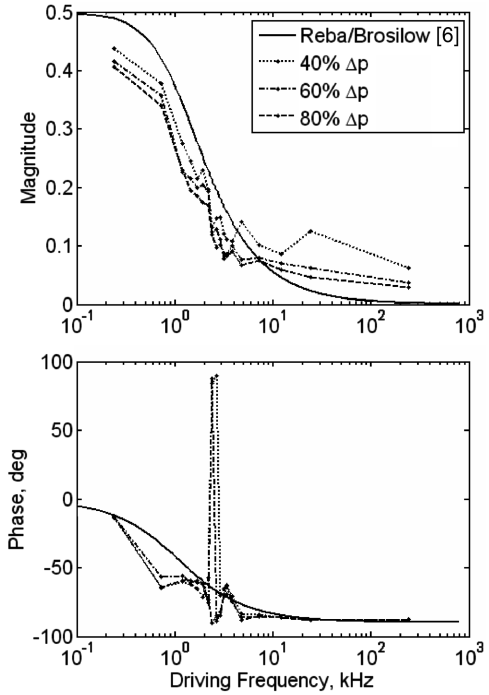

Fig. 13 Comparison of linear and nonlinear responses for all ε ($\bar{C}_D = 0.77$).

diameter ratios that were considered are $r/D = 0.005$, 0.01, 0.025, 0.05, 0.075, and 0.1.

The inlet rounding magnitude response in Fig. 14 shows a general decrease in magnitude as the inlet radius is increased. It is interesting to note that the overall magnitude of the response does not vary substantially as a function of r/D. The decrease in response with increased rounding is attributed to an increase in the discharge coefficient and a reduction in the size of the vena contracta region. Because this region effectively decreases the length of the orifice, as the vena contracta gets smaller, the effective length of the orifice increases, resulting in a less responsive injector. The phase response is much more dramatic for the various rounding conditions investigated. Even a small amount of rounding tends to remove the phase lead observed at the resonant condition, effectively driving the phase toward the −90- deg asymptotic value.

The inlet radius has a large impact on the mean discharge coefficient of the orifice. As the radius increases, the corner becomes less of an obtrusion into the flow and the flow can turn into the orifice without forming a large vena contracta region. For a very large inlet radius, the vena contracta virtually disappears, leading to a mean discharge coefficient approaching unity, as evidenced in Fig. 15.

The effect of orifice length on injector responsiveness was studied using the baseline injection conditions with peak-to-peak forcing at 40% of the mean Δp, with a forcing frequency of 2.4 Khz (the

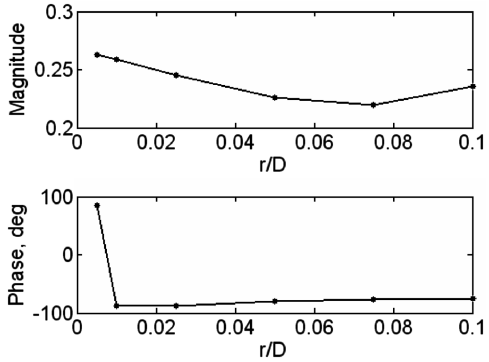

Fig. 14 Magnitude and phase responses for varying orifice inlet rounding.

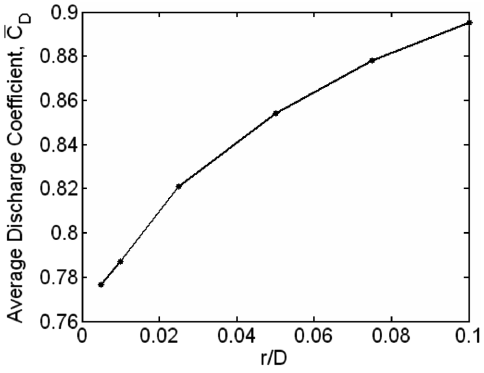

Fig. 15 Inlet corner radius effect on the discharge coefficient.

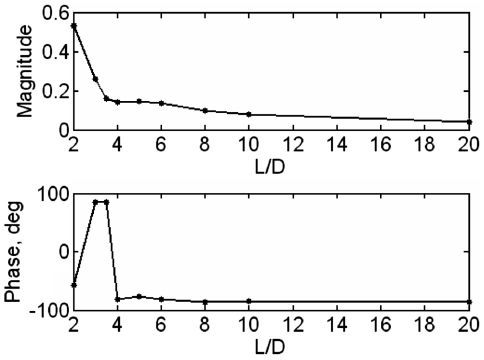

Fig. 16 Length effects for linear and nonlinear responses.

resonant condition for an L/D of 3). Orifice length-to-diameter ratios of $L/D = 2$, 3, 3.5, 4, 5, 6, 8, 10, and 20 were considered. As the injector length is increased, the inertance of the fluid inside the orifice becomes larger, and the linear theory [Eq. (18)] suggests that both the magnitude and phase responses should decrease.

Figure 16 depicts the nonlinear results. The magnitude response follows the theoretical trend suggested by the linear theory. The phase response shows a similar trend, with the exception of the resonance condition discussed in association with Fig. 10 for the $L/D = 3$ case. Apparently, this local resonance condition in the phase occurs over a narrow range of both frequency and orifice designs. Designs in this region will require additional attention with respect to the nonlinear phase response.

V. Conclusions

A series of laminar axisymmetric simulations are conducted to assess the nonlinear dynamic response of plain-orifice injectors. The linear theory is reviewed and it is shown that the linear results can be encapsulated into a single frequency response if the driving frequency is nondimensionalized by an injector frequency ω_i, which is closely related to the fluid transit time through the channel. Nonlinear simulations are performed over a wide range of frequencies for several different amplitudes and orifice geometries. At high Reynolds number conditions pertinent to most rocket applications, the instability of the vena contracta region formed near the inlet to the passage causes self-oscillations or an unforced response of the injector (i.e., these injectors produce unsteady flows even under the assumptions of steady inflow and outflow pressures). These natural pulsations are characterized by a frequency ω_n, which is dependent on the flow conditions and orifice L/D. For the flows investigated herein, the ratio of the two frequencies lies in the range of $0.1 < \omega_n/\omega_i < 0.35$, indicating that pulsations of the vena contracta typically occur on a timescale substantially larger than the orifice transit time.

Even for forced excitation as high as 80% of the mean pressure drop, the magnitude of the nonlinear response is bounded by the linear theory (except at high frequencies, in which the self-oscillations dominate the nonlinear results). A local resonance condition does exist when the driving frequency is near ω_n, but the magnitude of the response is still bounded by the linear theory in this region. The nonlinear phase response shows a similar behavior (bounded by linear theory), with the exception of a resonance condition near the ω_n frequency for some injector designs.

Parametric studies on driving pressure amplitude, Reynolds number, inlet radius, and orifice length are performed to observe trends in flow behavior. As the driving pressure amplitude increases, the dimensionless responsiveness of the injector decreases. Although rounding of the inlet has a significant response on the mean discharge coefficient, this parameter does not substantially influence the nonlinear dynamic response characteristics of the injector. Increasing the orifice length increased inertance/inertia within the passage and tends to decrease the overall response, assuming a fixed excitation frequency.

Acknowledgments

The authors gratefully acknowledge NASA for financial support of the project under the Constellation University Institutes Project, managed by Claudia Meyer and Jeff Rybak of NASA John H. Glenn Research Center at Lewis Field. The authors also acknowledge Marc Williams at Purdue University for his invaluable insight into the analysis of these results.

References

[1] Lefebvre, A., *Atomization and Sprays*, Hemisphere, New York, 1989.

[2] Ohrn, T. R., Senser, D. W., and Lefebvre, A. H., "Geometrical Effects on Discharge Coefficients for Plain Orifice Atomizers," *Atomization and Sprays*, Vol. 1, No. 2, 1991, pp. 137–157.

[3] Lichtarowicz, A., Duggins, R., and Markland, E., "Discharge Coefficients for Incompressible Non-Cavitating Flow Through Long Orifices," *Journal of Mechanical Engineering Science*, Vol. 7, No. 2, 1965, pp. 210–219.

[4] Nurick, W. H., "Liquid Rocket Engine Injectors," NASA SP-8089, 1976.

[5] Xu, C., Bunnell, R. A., and Heister, S. D., "On the Influence of Internal Flow Structure on Performance of Plain-Orifice Atomizers," *Atomization and Sprays*, Vol. 11, No. 4, 2001, pp. 335–350.

[6] Reba, I., Brosilow, C., "Combustion Instability: Liquid Stream and Droplet Behavior, Part 3: The Response of Liquid Jets to Large Amplitude Sonic Oscillations," U.S. Air Force Wright Air Development Center, WADC TR 59-720 Part 3, Wright–Patterson AFB, OH, 1960.

[7] Harrje, D., and Reardon, F., "Liquid Propellant Rocket Combustion Instability," NASA SP-194, 1972.

[8] Bazarov, V., and Yang, V., "Liquid-Propellant Rocket Engine Injector Dynamics," *Journal of Propulsion and Power*, Vol. 14, No. 5, Sept.–Oct. 1998, pp. 797–806.

[9] Muss, J., Johnson, C., and Nguyen, T., "User's Manual for Rocket Combustor Interactive Design (ROCCID 2003) and Analysis Computer Program," Sierra Engineering, Inc., Carson City, NV, 2004.

[10] Miesse, C., "The Effect of Ambient Pressure Oscillations on the Disintegration and Dispersion of a Liquid Jet," *Jet Propulsion*, Vol. 25, No. 10, Oct. 1955, pp. 525–530, 534.

[11] Bazarov, V. G., and Lyul'ka, L. A., "Nonlinear Interactions in Liquid Propellant Rocket Engine Injectors," AIAA Paper 98-4039, 1998.

[12] Rump, K. M., and Heister, S. D., "Modeling the Effect of Unsteady Chamber Conditions on Atomization Processes," *Journal of Propulsion and Power*, Vol. 14, No. 4, July–Aug. 1998, pp. 576–578.

[13] Heister, S. D., Rutz, M., and Hilbing, J., "Effect of Acoustic Perturbations on Liquid Jet Atomization," *Journal of Propulsion and Power*, Vol. 13, No. 1, 1997, pp. 82–88.

[14] Kim, B-D., and Heister, S. D., "Two-Phase Modeling of Hydrodynamic Instabilities in Coaxial Injectors," *Journal of Propulsion and Power*, Vol. 20, No. 32004, pp. 468–479.

[15] Kim, B-D., and Heister, S. D., "Three Dimensional Flow Simulations in the Recessed Region of a Coaxial Injector," *Journal of Propulsion and Power*, Vol. 21, No. 4, 2005, pp. 728–742.

[16] Canino, J. V., Heister, S. D., Sankaran, V., and Zakharov, S. I., "Unsteady Response of Recessed-Post Coaxial Injectors," 41st AIAA/ASME/SAE/ASEE Joint Propulsion Conference and Exhibit, Tucson, AZ, AIAA Paper 2005-4297, 2005.

[17] Cummings, A., "Acoustic Nonlinearities and Power Losses at Orifices," *AIAA Journal*, Vol. 22, No. 6, 1984, pp. 786–792.
[18] Jing, X., and Sun, X., "Discrete Vortex Simulation on The Acoustic Nonlinearity of an Orifice," *AIAA Journal*, Vol. 38, No. 9, 2000, pp. 1565–1572.
[19] Yakhot, A., Grinberg, L., and Nikitin, N., "Simulating Pulsatile Flows Through a Pipe Orifice by an Immersed-Boundary Method," *Journal of Fluids Engineering*, Vol. 126, Nov. 2004, pp. 911–918.
[20] Jocksch, A., and Gravett, C. P., "Effect of the Vortex Whistle on the Discharge Coefficient of Orifices," *AIAA Journal*, Vol. 42, No. 5, 2004, pp. 1048–1050.
[21] Howe, M. S., "On the Theory of Unsteady High Reynolds Number Flow Through a Circular Aperture," *Proceedings of the Royal Society of London*, Vol. 366, No. 1725, 1979, pp. 205–233.
[22] Dupere, I. D. J., and Dowling, A. P., "Absorption of Sound Near Abrupt Area Expansions," *AIAA Journal*, Vol. 38, No. 2, 2000, pp. 193–202.
[23] MacDonald, M. E., "On the Nonlinear Dynamic Response of Plain Orifice Atomizers/Injectors," M.S. Thesis, Purdue Univ., West Lafayette, IN, 2006.
[24] Peyret, R., and Taylor, T. D., *Computational Methods in Fluid Flow*, 2nd ed., Springer–Verlag, New York, 1983.
[25] Chen, Yongliang, Heister, and, Stephen, D., "A Numerical Treatment for Attached Cavitation," *Journal of Fluids Engineering*, Vol. 116, Sept. 1994, pp. 613–618.

D. Talley
Associate Editor